Tracking Hydrogen During Poly-Si/SiOx Contact Fabrication: An Infrared Spectroscopy Analysis of Si–H Bonds Configurations

Vincent Bocquet[1][https://orcid.org/0009-0003-4449-7733], Raphaël Cabal[1][https://orcid.org/0000-0001-6127-2024], Mickaël Albaric[1][https://orcid.org/0000-0002-0628-4580], Nevine Rochat[2][https://orcid.org/0000-0003-3574-4424], Raphaël Ramos[3][https://orcid.org/0000-0003-0627-6959], Jean-Paul Barnes[2][https://orcid.org/0000-0002-6547-6849], and Sébastien Dubois[1][https://orcid.org/0000-0002-3003-2981]

[1]CEA-INES, Université Grenoble Alpes, France

[2]CEA-LETI, Université Grenoble Alpes, France

[3]CEA-LITEN, Université Grenoble Alpes, France

Abstract. The hydrogenation step contributing to the high efficiencies (>25%) reached with poly-Si/SiOx passivated contacts solar cells is still poorly understood. In this study, Fourier transform infrared spectroscopy (FTIR) is used to follow the different bonding configurations of H during the fabrication process. The carrier lifetime degradation upon annealing is correlated to an important loss of Si–H bonds, from both the a-Si:H film and the SiOx interfaces. The subsequent hydrogenation step results in the formation of a small number of Si–H bonds near the crystalline silicon c-Si/SiOx interface, associated with the low stretching mode (LSM) and correlated to a significant lifetime improvement. These bonds feature a preferential orientation, as shown by polarized measurements.

Keywords: Silicon Solar Cells, Poly-Silicon, Hydrogen, TOPCon, FTIR

1. Introduction

Passivating contacts consisting of doped polycrystalline silicon on ultrathin silicon oxide (poly-Si/SiOx) have allowed solar cells to reach record efficiencies, both in laboratories and in the industry ($\eta \geq 26\%$ [1], [2], [3]). Their fabrication process generally includes a hydrogenation step, which highly contributes to their outstanding passivation quality [4]. Standard procedures involve the deposition of hydrogen-rich dielectrics, from which H diffuses to the interfaces and into the bulk, binding itself to structural defects and impurities, effectively passivating them. However, the exact phenomena at play are still unclear, and the presence of the poly-Si/SiOx stack complicates further the analysis. Moreover, several authors have linked H with light-and elevated temperature degradation (LeTID) [5] while others pointed out that when present in excess, H can damage the passivation quality in phosphorus doped passivating contacts [6].

In this work, FTIR is used to characterize the bonding configurations of H throughout the poly-Si contact fabrication process. The evolution of Si–H bonds is followed and correlated to carrier lifetime measurements. Previous FTIR studies have mainly focused on silicon heterojunction solar cells: monitoring bonding structures during a-Si:H deposition [7] and assessing the effects of deposition temperatures or hydrogen plasma treatments on film properties [8], [9]. But to the best of our knowledge, the only few reports of FTIR analyses on poly-Si/SiOx/c-Si stacks [10], [11] were performed in transmission mode, resulting in low signal-to-noise ratio. The contributions from the poly-Si/SiOx and SiOx/c-Si interfaces where Lehmann

et al. have shown H accumulates [12] could therefore not be observed. By using multiple internal reflexions (MIR) and attenuated total reflection (ATR) measurements techniques, a higher sensitivity can be obtained. This allows the observation of Si–H related peaks even in low-hydrogen content poly-silicon, as the one we deposited by low pressure chemical vapour deposition (LPCVD).

2. Experimental details

Symmetrical lifetime samples with SiO_x/poly-Si contacts were prepared on <100> chemical-mechanical polished Czochralski n-type silicon wafers ($\rho \sim 8\text{-}10$ Ω.cm). After a standard cleaning process (SC1, SC2), a chemical tunnel SiO_x was grown by ozone rinsing. This oxide was then densified directly in the LPCVD furnace where the intrinsic amorphous silicon deposition takes place (~ 10 or 30 nm, as verified by spectroscopic ellipsometry). Although part of the samples were doped via plasma immersion ion implantation, significant free carrier absorption prevented us to perform MIR-FTIR on these doped poly-Si, and this study will thus focus on the samples that were kept intrinsic. The annealing step was then carried out at 875°C for 30 min in N_2, inducing the crystallization of a-Si:H into poly-Si. Each wafer was cleaved into halves. One-half was put aside while the other underwent hydrogenation: a SiN_x:H layer was deposited by plasma enhanced chemical vapour deposition (PECVD). As it would have screened the sample during FTIR, SiN_x:H had to be removed by hydrofluoric acid (HF) dip. HF is, however, know to leave Si–H bonds on silicon surfaces [13]. For this reason, an additional controlled oxidation step was carried out. This process is summarized below in Fig. 2 (a).

The effective carrier lifetime value τ_{eff} was measured along the process by photo-conductance decay with the Sinton Instruments WCT-120 tool. Infrared (IR) characterizations were carried out using a Bruker IFS55 FTIR spectrometer and HgCdTe detector (600-4000 cm^{-1}). The IR beam was successively *s*- and *p*-polarized, allowing to probe the preferential orientations of the chemical bonds in the films [13]. The diagram in Figure 1 (a) depicts the 2 polarizations used alongside the MIR (b) and ATR (c) modes of measure.
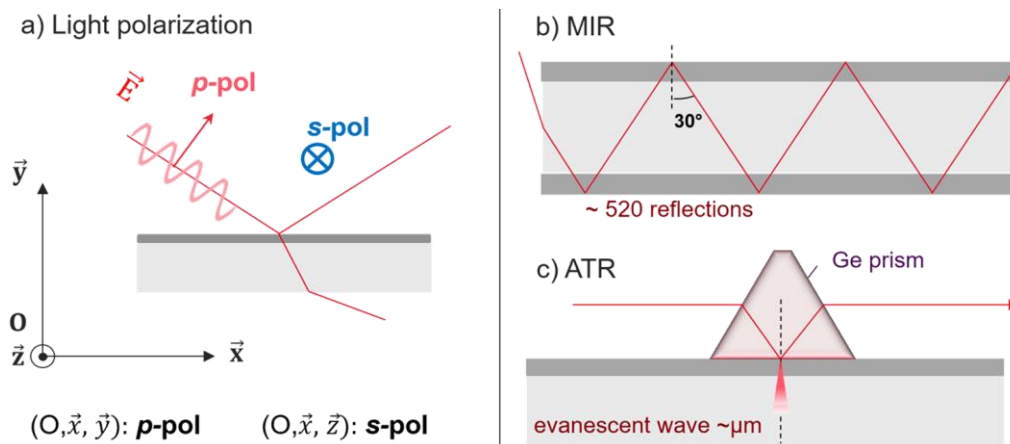

Figure 1. Schematic drawings of (a) transmission and reflection on a thin film in *p*- and *s*- polarizations, as indicated by the electric field vector direction. (b) Multiple internal reflection (MIR) and (c) attenuated total reflection (ATR) measurement modes.

In MIR measurements, light propagated through the wafers for 6 cm with an internal reflection angle of 30°. Only *s*-polarization was used here, as *p*-polarization in MIR is not consistent. MIR allowed excellent resolutions in the Si–H stretching mode (SM) region (1850-2300 cm-1), but the extended optical path through the wafer also led to IR absorption by the Si lattice vibrations; hence spectra are only available at $\omega > 1500$ cm^{-1}. In MIR, spectra are represented as differentials from a reference. The choice of the densified oxide spectrum for that purpose is explained in part 3.2. The ATR mode complemented the use of MIR: as light was directed at 65° onto a Ge prism, it ensured a single total reflection on the sample, with the evanescent

wave only probing the first micrometres of the sample. Therefore, almost no silicon-lattice absorption takes place, giving access to the full wavenumber range: [600, 4000] cm^{-1}. Moreover, both polarization modes can be used.

3. Results and discussion

3.1 Carrier lifetime evolution

Fig. 2 shows the effective carrier lifetime curves $\tau = f(\Delta n)$ throughout the fabrication steps. Lifetime values after (i)a-Si:H deposition start at τ ~150-300 µs. Annealing then significantly impairs the passivation quality, with τ ~25-30 µs. This is to be expected with intrinsic poly Si, as no field-effect passivation is present to counterbalance the deterioration of the chemical passivation caused by the annealing. Eventually, the SiN$_x$:H deposition enables these same wafers to reach τ ~500-900 µs, a higher value than the initial one. It seems that hydrogen, by binding itself to defects at the interface, allowed further improvement of the chemical passivation. FTIR, being sensitive to chemical bonds, should allow us to verify this hypothesis and determine the conformation of the bonds formed.
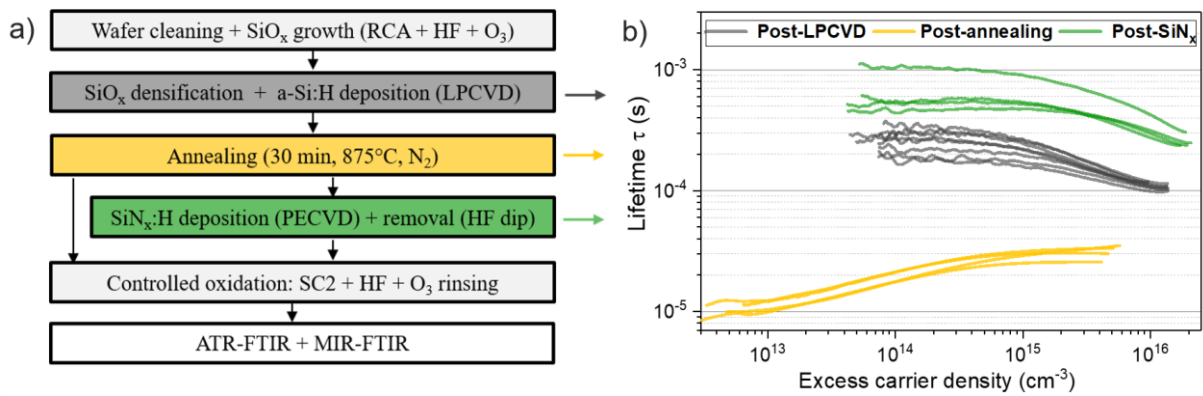

Figure 2. Evolution of the carrier lifetime curves along the fabrication process, as measured by photoconductance decay.

3.2 Tunnel oxide properties

As described above, our process starts by densifying the chemical SiO$_x$ formed by O$_3$ rinsing in the LPCVD tool. We first carried out a MIR-FTIR measurement (in *s*-pol) on the as-grown SiO$_{x\text{-chem}}$ and densified SiO$_{x\text{-dense}}$ samples. Fig. 3 (a) shows the effect of this densification step: it depicts the spectrum measured on the SiO$_{x\text{-dense}}$ taking the SiO$_{x\text{-chem}}$ as reference.
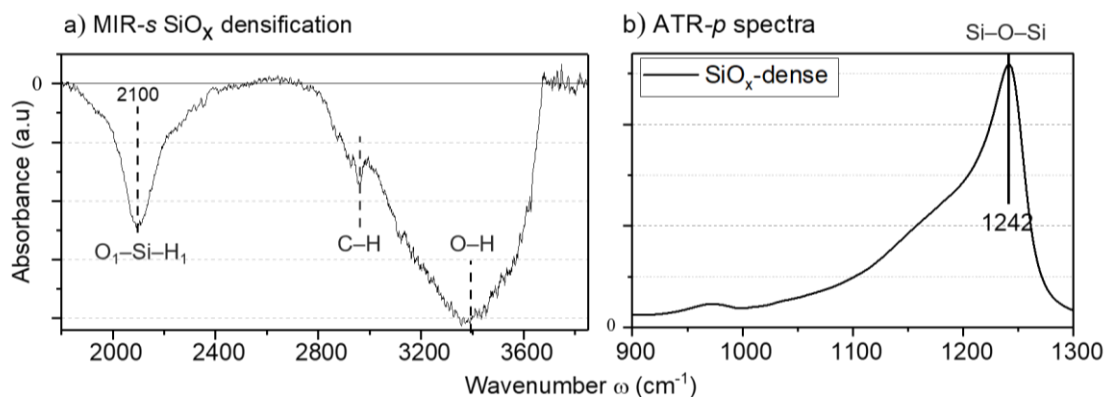

Figure 3. (a) MIR-FTIR spectrum of the SiO$_x$ densification in *s*-polarization. (b) ATR-FTIR spectra of the resulting SiO$_{x\text{-dense}}$ in the Si–O–Si stretching mode region.

Two main peaks are present: the Si–H stretching mode (SM) at 2100 cm^{-1} and the well-known broad O–H band at 3000~3300 cm^{-1}. The 2100 cm^{-1} peak is attributed to O_1–Si–H_1: because of its electronegativity, oxygen shifts the standard ω_{Si-H1} ~2000 cm^{-1} to higher wavenumbers by induction [14]. C–H bonds are also detected and reflect a probable contamination during wafer transport. In conclusion, the densification seems to induce a loss of hydrogen from the oxide and its surface (probable desorption of H_2O from the surface).

Fig. 3 (b) shows the Si–O–Si SM region of the ATR-*p* spectrum of the resulting $SiO_{x-dense}$. The shape and position of the Si–O–Si peak (Longitudinal optical antisymmetric stretching vibration LOAS1 ~1241 cm^{-1}) indicate the structure of our $SiO_{x-dense}$ is more similar to a thermal oxide than an annealed chemical oxide [15] (for comparison: $\omega_{Si-O-Si}$ ~1210 cm^{-1} for our SiO_{x-chem} and $\omega_{Si-O-Si}$~1230 cm^{-1} for an annealed SiO_{x-chem} in [15]). Apart from the surface O–H band, it is the only salient feature of the spectrum. This shows that after densification, no bonded hydrogen is present in the oxide, justifying the use of $SiO_{x-dense}$ spectrum as reference for all other MIR-spectra in the rest of the study.

3.3 MIR-FTIR Observations

3.3.1 Peak attribution

All MIR spectra were calculated with thermally densified SiO_x as a reference. The focus will be the stretching mode region: [1900, 2300] cm^{-1} which has been shown to be particularly instructive [16]. Fig. 4 (a) features the spectrum measured for the post-LPCVD sample and its peak deconvolution.
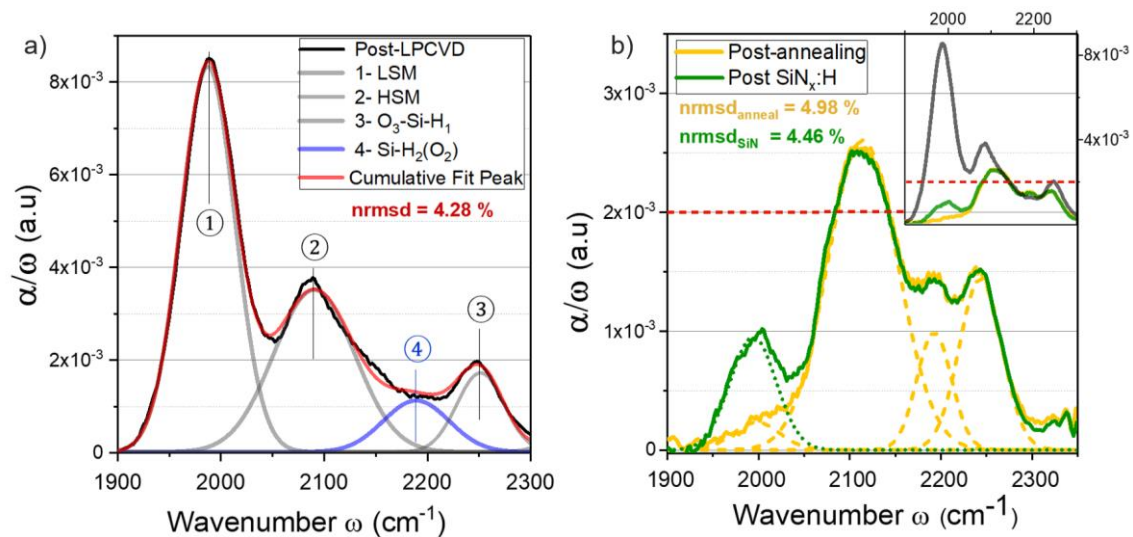

Figure 4. MIR-FTIR spectra of poly-Si/SiO_x contacts at different fabrication steps: (a) Peak identification for the post-LPCVD sample results in a 4-Gaussian model. (b) This model is applied to post-annealing and post-SiN_x:H samples. The inset at the top right-hand corner features the three spectra for size comparison.

Three peaks are directly apparent:

(1) 1990 cm^{-1}: the low stretching mode (LSM), associated in the literature to monohydrides Si–H_1 isolated or at vacancies in a-Si:H or microcrystalline silicon (µc-Si:H) [17], [18]
(2) 2090 cm^{-1}: the high stretching mode (HSM), reported as Si–H_2 or as Si–H_1 at void surfaces [17], [18] in a-Si:H or µc-Si:H
(3) 2250 cm^{-1}: Monohydrides in oxidized environment: O_3–Si–H_1. It has been reported in a large variety of environments: at c-Si surfaces [19], c-Si/a-Si interfaces [7] as well as in bulk µc-Si:H [20].

The presence of a 4th peak at 2190 cm^{-1} (in blue in Figure 4 (a)) explains the asymmetry of the second peak and is directly visible after annealing, as one can notice in Fig. 4 (b). This peak was attributed to dihydrides in oxidized environment: $Si–H_2(O_2)$ in the same environment as $O_3–Si–H_1$ [19], [7], [20]. The deconvolution in 4-Gaussians proved to be consistent for all samples, with low normalized root-mean deviation (nrmd) values (< 7%).

3.3.2 Quantitative analysis

A semi-quantitative analyse can then be applied by integrating the peaks following the procedure developed by Brodsky et al. [17]:

$$N_{bonds} \propto I = \int \left(\frac{\alpha}{\omega}\right) d\omega \qquad (1)$$

I is the integrated absorbance, with α the absorption coefficient $\alpha = -\ln(T)$. $T(\omega)$ is the transmittance measured, $\omega = 1/\lambda$ the wavenumber.

If we consider that the LSM and HSM peaks in the post-LPCVD spectrum stem mainly from the a-Si:H layer itself, we can use the procedure and constants in [18], [21], [22] to estimate the hydrogen concentration in the a-Si layer. This yields [H] ~ 0.5 ± 0.1%. This assumption is nevertheless no longer valid after annealing, as H is redistributed near the c-Si/SiO$_x$ interface (shown later). Fig. 5 gives an idea of the evolution of the number of each Si–H conformation throughout the process. The two oxide-related peaks ($O_3–Si–H_1$ and $Si–H_2(O_2)$) are lumped together as I$_{oxide}$ to simplify reading.
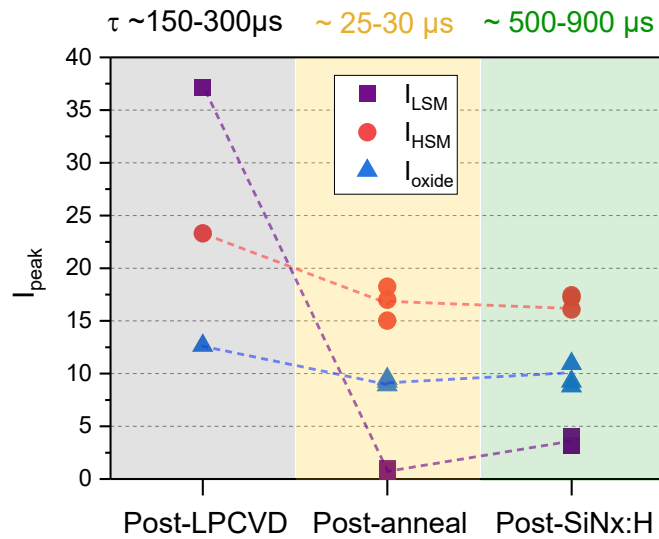

Figure 5. Evolution of I $\propto$ N$_{bonds}$ along the poly-Si/SiO$_x$ contacts fabrication.

It can be observed that annealing is causing a clear and significant loss of Si–H bonds, notably in LSM (-96%) and HSM (-28%), and to a lesser extent for the oxide peaks (-27%). Conversely, the hydrogenation step is only visible through the increase in LSM (×3 to ×6), and post-SiN$_x$/post-annealing spectra are otherwise similar. We can thus assume this LSM increase is causing the dramatic lifetime improvement. This therefore brings the following question: what makes post-SiN$_x$:H lifetime exceed its post-LPCVD level, when the LSM peak of the latter is much larger (×10)?

3.3.3 Interpretation

We explain it as follows: the LSM encompasses Si–H$_1$ of various sources. During the annealing, the Si–H loss (both LSM and HSM) should originate mainly from the a-Si:H. As it crystal-

lizes into poly-Si, the H that passivated dangling bonds (DB) is exo-diffused. SIMS observations by other groups seem to concur [23]. On the other hand, the LSM appearing upon SiN_x deposition is coming mainly from the interface. This statement is supported by 3 observations:

(1) A shift in ω_{LSM} is observed between post-LPCVD (1988 cm^{-1}) and the other samples (2000-2010 cm^{-1}), indicating the change is not only quantitative but also qualitative.

(2) An experimental test was carried out with different poly-Si thicknesses (30 vs 10 nm) to assess the volume/interface contributions of $Si–H_x$ peaks. The MIR spectra are shown just below in Fig. 6.
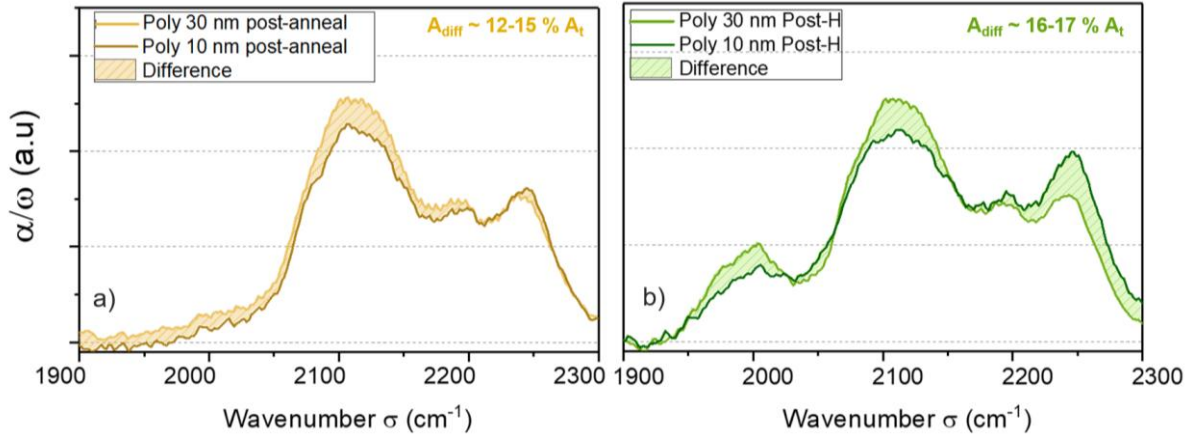

Figure 6. Comparison of spectra between a 10 nm and a 30 nm-thick poly-Si after (a) annealing and (b) after hydrogenation. Difference in area stays below 20% in both cases.

Although the poly-Si was three-times thicker, the integrated areas only differs by 12 to 17%. This demonstrates that after annealing, most of $Si–H_x$ bonds are concentrated either at the $c-Si/SiO_x/poly-Si$ interfaces or at the surface of the samples.

(3) Finally, we know that the lifetime drop caused by annealing is coming from an interface degradation (indeed, doped poly-Si does not see such a drop, as field-effect passivation counterbalances it). So H should necessarily act on the interface itself.

3.4 ATR-FTIR Observations

FTIR-ATR spectra are presented in Fig. 5, respectively in *s*- and *p*-polarizations. To get a quantitative metric, the ratio of the absorbances A_p/A_S is also plotted in 5.c). All spectra were fitted with the 4-Gaussians model (Fig. 4 (a)).
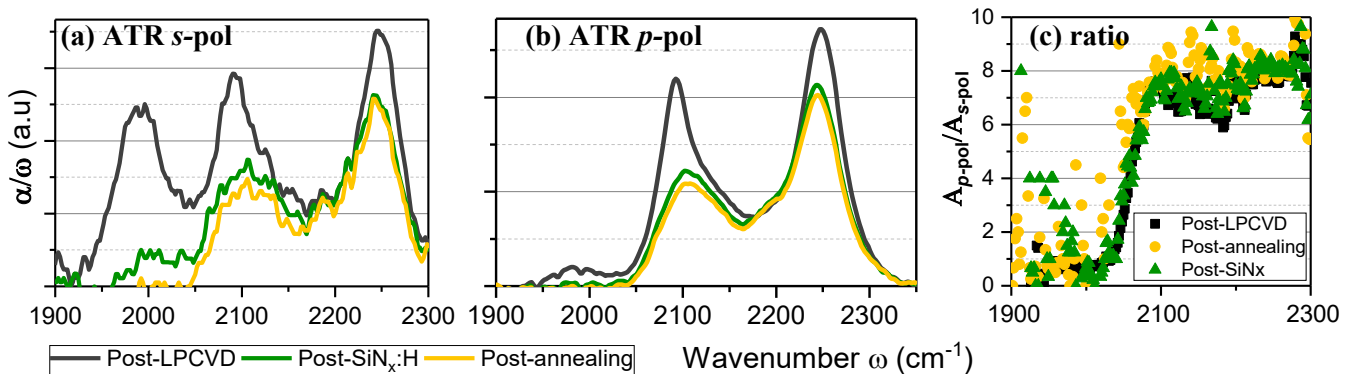

Figure 7. ATR spectra measured in (a) s- and (b) p- polarization at the different fabrication steps. (c) Absorbances ratio p/s.

The main insights are:

(1) Peaks observed in *s*-polarization ATR are the same as in MIR. However, their respective areas changed, with stronger oxide peaks. But the evolution is consistent from one sample to another (i.e. $I_{ATR-LSM}/I_{MIR-LSM}$ is the same for all samples). This can come from oxidation of the samples (as ATR measurements were carried out 3 months later than MIR), or from an increased sensitivity of ATR for these modes.

(2) In *p*-polarization, the LSM peak almost disappears. This is clearly shown in Fig. 5(c) where the A_p/A_S ratio reaches ~0.6-0.8 for this single peak. For the other peaks, *p*-pol is more sensitive than *s*-pol so A_p/A_s ~ 6-8. This implies that LSM Si–H_1 bonds show a preferential orientation. Similar reports exist following HF treatments of c-Si, but where *s*-pol disappears [13], indicating a direction of the bonds perpendicular to the c-Si surface. The only occurence of *p*-pol was reported for the Si–H wagging mode in a thick columnar a-Si structure [24].

4. Conclusion and perspectives

A thorough analysis of the evolution of H bonding conformations during poly-Si/SiO$_x$ contacts elaboration has been given. Combining MIR-/ATR-FTIR in *s*- and *p*-polarizations, we show that the lifetime decrease upon annealing can be correlated to H exo-diffusion and that this H is mainly coming from the a-Si:H film. The hydrogenation step then leads to a creation of Si–H_1 bonds at the c-Si/SiO$_x$/poly-Si interfaces. These very same bonds seem to show a preferential orientation in space. Using complementary characterization methods such as H profiling and Electron Spin Resonance, we hope to verify and confirm these observations in our next study.

Data availability statement

The data collected supporting the findings are available from the corresponding author upon reasonable request.

Author contributions

Vincent Bocquet: Writing – original draft, Conceptualization, Methodology, Formal Analysis, Investigation; Raphaël Cabal: Supervision, Conceptualization, Visualization, Resources, Review; Mickael Albaric: Supervision, Conceptualization, Review; Nevine Rochat and Raphaël Ramos: FTIR characterization, Formal Analysis; Jean-Paul Barnes: Supervision, Review; Sébastien Dubois: Review, Resources.

Competing interests

The authors declare no competing interests.

References

1. A. Richter *et al.*, "Design rules for high-efficiency both-sides-contacted silicon solar cells with balanced charge carrier transport and recombination losses," Nat Energy, vol. 6, no. 4, Art. no. 4, pp. 429–438, Apr. 2021, doi: 10.1038/s41560-021-00805-w.
2. C. Hollemann, F. Haase, S. Schäfer, J. Krügener, R. Brendel, and R. Peibst, "26.1%-efficient POLO-IBC cells: Quantification of electrical and optical loss mechanisms," Prog. Photovolt: Res and Appl., vol. 27, no. 11, pp. 950–958, 2019, doi: 10.1002/pip.3098.

3. "JinkoSolar's High-efficiency N-Type Monocrystalline Silicon Solar Cell Sets Our New Record with Maximum Conversion Efficiency of 26.4% | JinkoSolar." https://ir.jinkosolar.com/news-releases/news-release-details/jinkosolars-high-efficiency-n-type-monocrystalline-silicon-2 (accessed Mar. 15, 2023).

4. R. Chen *et al.*, "24.58% efficient commercial n-type silicon solar cells with hydrogenation." Prog. Photovolt: Res Appl., vol. 29, no. 11, pp. 1213–1218, Nov. 2021, doi: 10.1002/pip.3464.

5. D. Chen *et al.*, "Hydrogen induced degradation: A possible mechanism for light- and elevated temperature- induced degradation in n-type silicon," Sol. Energy Mater. Sol. Cells, vol. 185, pp. 174–182, Oct. 2018, doi: 10.1016/j.solmat.2018.05.034.

6. D. Kang *et al.*, "Optimum Hydrogen Injection in Phosphorus-Doped Polysilicon Passivating Contacts," ACS Appl. Mater. Interfaces, vol. 13, no. 46, pp. 55164–55171, Nov. 2021, doi: 10.1021/acsami.1c17342.

7. H. Fujiwara and M. Kondo, "Real-time monitoring and process control in amorphous⁄crystalline silicon heterojunction solar cells by spectroscopic ellipsometry and infrared spectroscopy," Appl. Phys. Lett., vol. 86, no. 3, p. 032112, Jan. 2005, doi: 10.1063/1.1850612.

8. Y. Zhao *et al.*, "Effects of (i)a-Si:H deposition temperature on high-efficiency silicon heterojunction solar cells," Prog. Photovolt: Res Appl., Sept. 2022, 1-11 doi: 10.1002/pip.3620.

9. A. Soman and A. Antony, "A critical study on different hydrogen plasma treatment methods of a-Si: H/c-Si interface for enhanced defect passivation," Appl. Surf. Sci., vol. 553, p. 149551, Jul. 2021, doi: 10.1016/j.apsusc.2021.149551.

10. T. N. Truong *et al.*, "Hydrogen-Assisted Defect Engineering of Doped Poly-Si Films for Passivating Contact Solar Cells," ACS Appl. Energy Materials, vol. 2, no. 12, pp. 8783–8791, 2019, doi: 10.1021/acsaem.9b01771.

11. W. Chen *et al.*, "Influence of PECVD deposition temperature on phosphorus doped poly-silicon passivating contacts," Sol. Energy Mater. Sol. Cells, vol. 206, p. 110348, Mar. 2020, doi: 10.1016/j.solmat.2019.110348.

12. M. Lehmann *et al.*, "Analysis of hydrogen distribution and migration in fired passivating contacts (FPC)," Sol. Energy Mater. Sol. Cells, vol. 200, p. 110018, Sep. 2019, doi: 10.1016/j.solmat.2019.110018.

13. H. Ogawa, K. Ishikawa, C. Inomata, and S. Fujimura, "Initial stage of native oxide growth on hydrogen terminated silicon (111) surfaces," J Appl. Phys., vol. 79, no. 1, pp. 472–477, Jan. 1996, doi: 10.1063/1.360853.

14. G. Lucovsky and W. B. Pollard, "Local bonding of oxygen and hydrogen in a-Si:H:O thin films," J. Vac Sci. Tech. A, vol. 1, no. 2, pp. 313–316, Apr. 1983, doi: 10.1116/1.572121.

15. D. Rouchon, N. Rochat, F. Gustavo, A. Chabli, O. Renault, and P. Besson, "Study of ultrathin silicon oxide films by FTIR-ATR and ARXPS after wet chemical cleaning processes," Surf. Interf. Analysis, vol 34, no. 1, pp. 445–450, 2002, doi: 10.1002/sia.1335.

16. A. H. M. Smets, T. Matsui, M. Kondo, and M. C. M. van de Sanden, "The hydride stretching modes of hydrogenated vacancies in amorphous and nanocrystalline silicon: A helpful tool for material characterization," in 2009 34th IEEE Photovoltaic Specialists Conference (PVSC), Jun. 2009, pp.721–724. doi: 10.1109/PVSC.2009.5411182.

17. M. H. Brodsky, M. Cardona, and J. J. Cuomo, "Infrared and Raman spectra of the silicon-hydrogen bonds in amorphous silicon prepared by glow discharge and sputtering," Phys. Rev. B, vol. 16, no. 8, pp. 3556–3571, Oct. 1977, doi: 10.1103/PhysRevB.16.3556.

18. A. H. M. Smets, W. M. M. Kessels, and M. C. M. van de Sanden, "Vacancies and voids in hydrogenated amorphous silicon," Appl. Phys. Lett., vol. 82, no. 10, Art. no. 10, Mar. 2003, doi: 10.1063/1.1559657.

19. M. Niwano, J. Kageyama, K. Kurita, K. Kinashi, I. Takahashi, and N. Miyamoto, "Infrared spectroscopy study of initial stages of oxidation of hydrogen-terminated Si surfaces stored in air," J. Appl. Phys., vol. 76, no. 4, pp. 2157–2163, Aug. 1994, doi: 10.1063/1.357627.

20. A. C. Bronneberg, A. H. M. Smets, M. Creatore, and M. C. M. van de Sanden, "On the oxidation mechanism of microcrystalline silicon thin films studied by Fourier transform infrared spectroscopy," J. Non. Cryst. Solids, vol. 357, no. 3, pp. 884–887, Feb. 2011, doi: 10.1016/j.jnoncrysol.2010.11.001.

21. G. Amato, G. Della Mea, F. Fizzotti, C. Manfredotti, R. Marchisio, and A. Paccagnella, "Hydrogen bonding in amorphous silicon with use of the low-pressure chemical-vapor-deposition technique," Phys. Rev. B, vol. 43, no. 8, pp. 6627–6632, Mar. 1991, doi: 10.1103/PhysRevB.43.6627.

22. A. A. Langford, M. L. Fleet, B. P. Nelson, W. A. Lanford, and N. Maley, "Infrared absorption strength and hydrogen content of hydrogenated amorphous silicon," Phys. Rev. B, vol. 45, no. 23, pp. 13367–13377, Jun. 1992, doi: 10.1103/PhysRevB.45.13367.

23. S. Choi *et al.*, "Structural evolution of tunneling oxide passivating contact upon thermal annealing," Sci Rep, vol. 7, no. 1, Art. no. 1, Oct. 2017, doi: 10.1038/s41598-017-13180-y.

24. J. D. Webb *et al.*, "Anisotropy in Hydrogenated Amorphous Silicon Films as Observed Using Polarized Ftir-Atr Spectroscopy," MRS Online Proceedings Library (OPL), vol. 557, p. 311, ed 1999, doi: 10.1557/PROC-557-311.